Full spectral XANES imaging using the Maia detector array as a new tool for the study of the alteration process of chrome yellow pigments in paintings by Vincent van Gogh

Letizia Monico,[1,2,] Koen Janssens,[2] Matthias Alfeld,[3] Marine Cotte,[4,5] Frederik Vanmeert,[2] Chris G. Ryan,[6] Gerald Falkenberg,[3] Daryl L. Howard,[7] Brunetto Giovanni Brunetti,[1] Costanza Miliani.[1]*

[1] Institute of Molecular Science and Technologies (ISTM), National Research Council (CNR) and Centre SMAArt, c/o Department of Chemistry, Biology and Biotechnologies, University of Perugia, via Elce di Sotto 8, 06123 Perugia, Italy.

[2] University of Antwerp, Department of Chemistry, Groenenborgerlaan 171, 2020 Antwerp, Belgium.

[3] Deutsches Elektronen-Synchrotron, Notkestraße 85, 22603 Hamburg, Germany.

[4] European Synchrotron Radiation Facility, Avenue des Martyrs 71, 38000 Grenoble, France.

[5] Laboratoire d'Archéologie Moléculaire et Structurale, CNRS-UPMC, UMR 8220, place Jussieu 4, 75005 Paris, France.

[6] Commonwealth Scientific and Industrial Research Organisation, Minerals Research Flagship, Normanby Road, Clayton, Victoria 3168, Australia.

[7] Australian Synchrotron, 800 Blackburn Road, Clayton, Victoria 3168, Australia.

* Correspondance: letizia.monico@uantwerpen.be

†Electronic supplementary information (ESI) available.

ABSTRACT

A combination of synchrotron radiation (SR) micro X-ray fluorescence (μ-XRF) and XRF mode X-ray absorption near edge structure (XANES) measurements at the Cr K-edge already allowed us to establish that the photo-reduction of chromates to Cr(III)-compounds is the cause of darkening of chrome yellow pigments ($PbCr_{1-x}S_xO_4$, $0 \leq x \leq 0.8$) in a number of paintings by Vincent van Gogh and in corresponding artificially aged paint models. A silicon drift detector (SDD) was employed to record the Cr-K XRF radiation in these X-ray micro beam-based measurements.

However, in view of the limited count rate capabilities and collection solid angle of a single device, μ-XRF and μ-XANES employing single element SDDs (or similar) are primarily suited for collection of spectral data from individual points. Additionally, collection of XRF maps via point-by-point scanning with relatively long dwell times per point is possible but is usually confined to small areas.

The development of the 384 silicon-diode array Maia XRF detector has provided valuable solutions in terms of data acquisition rate, allowing for full-spectral (FS)-XANES imaging in XRF mode, *i.e.,* where spectroscopic information is available at each pixel in the scanned map.

In this paper, the possibilities of SR Cr K-edge FS-XANES imaging in XRF mode using the Maia detector is examined as a new data collection strategy to study the speciation and distribution of alteration products of lead chromate-based pigments in painting materials. The results collected from two micro-samples taken from two Van Gogh paintings and an aged paint model show the possibility to perform FS-XANES imaging in practical time frames (from several minutes to a few hours) by scanning regions of the same order size of samples (more than 500 μm). The sensitivity and capabilities of FS-XANES imaging in providing representative chemical speciation information at the microscale (spatial resolution from ~2 to 0.6 μm) over the entire scanned area

are demonstrated by the identification of $Cr(OH)_3$, Cr(III)-sulfates and/or Cr(III)-organometallic compounds in the corresponding phase maps, as alteration products.

Comparable Cr-speciation results were obtained by performing equivalent higher spatial resolution SR μ-XRF/single point μ-XANES analysis using a more conventional SDD from smaller region of interest of each sample. Thus, large area XRF mode FS-XANES imaging (Maia detector) is here proposed as a valuable and complementary data collection strategy in relation to "zoomed-in" high resolution μ-XRF mapping and single point μ-XANES analysis (SDD).

1. INTRODUCTION

During the last decades, synchrotron radiation (SR)-based X-ray microprobe techniques, such as micro X-ray fluorescence (μ-XRF) and X-ray absorption near edge structure (XANES) methods (in point analysis or in mapping mode), have been successfully employed for the study of the degradation pathways of artists' pigments due to their valuable capabilities to provide information on the speciation and on the distribution of the secondary compounds from micrometer- to nanometer-scale.[1,2,3]

In many cases, the chromatic alteration encountered in specific areas of paintings from Antiquity to late 18th century can be ascribed to redox processes and/or modification of metal coordination of some inorganic compounds, such as the pigments cinnabar (HgS),[4,5] smalt (a potash glass in which the color stems from cobalt ions),[6,7] Prussian blue ($MFe^{III}[Fe^{II}(CN)_6] \cdot xH_2O$, with M= K^+, NH_4^+ or Na^+),[8,9] copper resinate [10] and verdigris [11] (both green copper organo-metallic compounds). Regarding late 19th-early 20th century yellow pigments, the photo-oxidation of the original CdS (cadmium yellow) to $CdSO_4$ was proposed as the mechanism responsible for fading of some yellow areas in masterpieces by Ensor,[12] Van Gogh[13] and Matisse,[14] whereas the photo-reduction of the zinc yellow pigment ($K_2O \cdot 4ZnCrO_4 \cdot 3H_2O$) to ochre-green Cr(III)-compounds was identified as a cause of the chromatic alteration in a painting by Seurat.[15] A light induced reduction is also the cause of darkening in selected chrome yellow paint areas ($PbCr_{1-x}S_xO_4$, $0 \leq x \leq 0.8$) in a number of Van Gogh paintings.[16,17] Studies of photochemically aged paint models composed of different chrome yellow varieties revealed that the reduction of Cr(VI) is favored when the pigment is present in the S-rich orthorhombic $PbCr_{1-x}S_xO_4$ (with x>0.4) form.[18,19]

In all the above mentioned studies, μ-XRF maps and single point μ-XANES spectra in XRF mode were collected by means of traditional energy dispersive (ED)-X-ray detectors [*e.g.,* silicon drift detectors (SDDs)/germanium solid state detectors]. These systems reach spectral energy

resolutions down to about 140 eV FWHM at the Mn K_α-line (5.9 keV) but are characterized by a limited count rate capability that usually can be situated up to 5×10^5 counts/s but that may increase to $3\text{-}4\times 10^6$ counts/s for other recently developed devices.[20,21] Therefore, during mapping (of XRF signals collected while raster scanning the sample) and XANES (involving scanning the energy of the primary beam across the absorption edge of the element of interest) experiments, fairly long dwell times per point/pixel or point/energy (*i.e.,* 0.1-1 s) must be respected.[22,23,24] This can result in extended scanning times (typically of the order of several hours per map and a few minutes per XANES spectrum) and relatively high X-ray doses impinging on the materials. The latter may increase the probability of beam-induced damage in the examined specimen.[25] These non-optimal characteristics of traditional ED-XRF detectors frequently confine the data acquisition in μ-XRF mapping experiments to few and relatively small regions of interest within the sample, with the consequence that the obtained results might not be representative of the entire material. These limitations become even more stringent when XANES mapping experiments are undertaken. A typical experiment of this kind consists in analysing one or more areas of interest by recording μ-XRF maps at a few (~2-5) different energy values around an absorption edge. Discriminating energies can be selected on the basis of the XANES spectral features of the compounds to be investigated; through manipulation of the resulting XRF maps, a set of chemical state distributions can be obtained. Mapping measurements of this kind are usually combined with collection of single point XANES spectra in XRF mode at a limited number of locations, thought to be representative of the entire map. Via such a procedure, however, the full spectral XANES response of all examined points in the mapped area is not recorded. Thus, it is not excluded that the presence of specific species of the element of interest in a subarea of the map may be completely overlooked.

By employing "fast" XRF detectors it is possible to overcome some of the above-mentioned limitations of traditional ED-XRF data acquisition systems. In this category, the Maia-384 massively parallel detector [jointly developed by the Commonwealth Scientific and Industrial Research Organization (CSIRO, Australia) and the Brookhaven National Laboratory (BNL, USA)] occupies a central position.[26,27,28] The system consists of an annular array of 384 silicon-diode detectors positioned in a backscatter geometry with respect to the incident X-ray beam; this geometry ensures that a large (~1.3 sr) solid-angle is subtended. An approach based on an event-mode data collection with real-time processing capabilities allows to record maps with a minimum dwell time down to ~0.05 ms/pixel and a total count-rate capacity greater than 10 M/s while avoiding readout overheads. A real-time full-spectral elemental deconvolution can be obtained through an integrated algorithm based on a matrix transform method called Dynamic Analysis (DA).[29]

The Maia detector has found wide application for performing two-dimensional micrometer-scale resolution elemental mapping experiments over large areas of materials of interest in different scientific fields, such as earth and environment science,[30,31,32,33] biology,[34,35] medicine,[36,37] and cultural heritage.[38] It has also allowed micro-tomography[39,40,41] and XRF-mode XANES imaging[42,43,44,45] to be successfully conducted on biological and environmental samples in practical time frames. During XRF mode XANES-imaging of this type, chemical speciation information is obtained *via* fast, sequential acquisition of a series of XRF images at the micrometer scale while small incremental changes in energy (E) are made across the absorption edge of the element of interest. After DA elemental deconvolution, the XANES spectra can be extracted at each pixel from the E-stack of images and chemical state maps can be calculated by employing a linear combination fitting procedure against a set of reference spectra. This type of full spectral (FS)-XANES imaging appears in principle optimal for the study of complex and heterogeneous samples

such as degraded paint micro-samples. However, so far, this state-of-the art detector technology has never been employed in the context of artist pigments' alteration studies.

In this paper, Cr K-edge FS-XANES imaging in XRF mode is proposed as a new strategy for studying the nature and distribution of alteration products of lead chromate-based yellow pigments in painting materials. The aims of the paper are threefold: i) outline the technical advantages and drawbacks in using either FS-XANES imaging or μ-XRF mapping/single point μ-XANES investigations in the specific context of the study of altered chrome yellow paints; ii) evaluate whether or not FS-XANES imaging can contribute to a more representative and reliable identification of the Cr-based alteration compounds and their spatial distribution (through the collection of XANES spectral profiles from all locations in the examined area); iii) assess if FS-XANES imaging may be used as a reliable method for quantitatively determining the abundance of different Cr-species and compare its performance to that of more conventional single point μ-XANES analysis.

For these purposes, in the following sections, we present and discuss a comparison between FS-XANES imaging data obtained at the Cr K-edge using the Maia X-ray detector and corresponding μ-XRF mapping/single point μ-XANES results acquired by means of a more conventional SDD. Data were collected during the study of two altered chrome yellow paint micro-samples taken from two paintings by Vincent Van Gogh: *Falling leaves (Les Alyscamps)* (Kröller-Müller Museum, Otterlo, NL) and *The Bedroom* (Van Gogh Museum, Amsterdam, NL). In addition, similar data recorded from a relevant photochemically aged chrome yellow paint model are also described.

2. EXPERIMENTAL

2.1 Resin-embedded original paint micro-samples and photochemically aged model paint.

Investigations were performed on two resin-embedded paint micro-samples taken earlier from darkened chromium-based yellow areas of the following paintings by Van Gogh: *Falling leaves (Les Alyscamps)* (sample 224/1) and *The Bedroom* (sample F482/8) (Figures 1A-2A). The sampling locations of these paints are reported in Figure S1 of the ESI†.

Previous SEM-EDX, micro-FTIR, micro-Raman and SR micro-X-ray diffraction analysis of the selected samples allowed to demonstrate that chrome yellow is present as a $PbCr_{1-x}S_xO_4$ (x~0.5) co-precipitate in sample 224/1, while in F482/8 it occurs as $PbCrO_4$.[46,47]

Measurements were also carried out on a paint model that was prepared by mixing $PbCr_{0.2}S_{0.8}O_4$ with linseed oil in a 4:1 weight ratio and by applying the mixture on a polycarbonate microscope slide. In line with previous papers,[17,19,47] this sample is designated henceforth as S_{3D}. The paint model was irradiated using a commercial light source emitting radiation above 400 nm for 21 days. The measured illuminance at the sample position was about 3×10^5 lux. The aged material was prepared and analyzed as a thin section of about 10 μm thickness (see below, Figures 8A-C).

2.2. SR-based X-ray investigations at the Cr K-edge.

Synchrotron X-ray experiments at the Cr K-edge were performed in two modes: (i) conventional μ-XRF mapping at different energies combined with the acquisition of a few single point μ-XANES spectra and (ii) FS-XANES imaging in XRF mode. Investigations (i) were carried out at the X-ray microscope beamline ID21 of the European Synchrotron Radiation Facility (ESRF, Grenoble, FR)[48] by means of a SDD, while measurements (ii) were carried out at the X-ray fluorescence microscopy (XFM) beamline of the Australian Synchrotron (AS, Melbourne, AUS)[49] and at the Hard X-ray micro/nano-probe beamline P06 of the Deutsches Elektronen-Synchrotron (DESY, Hamburg, DE)[26] using the Maia-384A and Maia-384B detectors, respectively. An overview of the

experimental set-up and the conditions used at these three SR end stations are reported in Tables 1-2. Further details are provided in the following sections.

2.2.1. XFM beamline (AS). Original paint micro-samples were analyzed in the 5.96-6.09 keV energy range using a monochromatic primary beam (about $\Delta E/E = 10^{-4}$) produced by means of a Si(111) fixed-exit double-crystal monochromator. Kirkpatrick-Baez (KB) mirrors were used to focus the beam to a spot size of about 2×2 μm² (h×v). The beam drift over a 24 hours period is within 3 μm in the horizontal and vertical directions, respectively, and the beam is stable within 1 μm vertical and 1 μm horizontal in the 5.96-6.09 keV energy range.

The Maia-384A detector had a 375 eV spectral energy resolution at the Mn K_{α}-line (5.9 keV); scanning was performed with dwell time between 0.5-2 ms/pixel. The XRF signal was collected in a backscatter geometry with respect to the incident beam with a solid angle of ~1.3 sr.[28]

A stack of 126 μ-XRF maps was recorded at around the Cr K-edge using the following energy increments: (i) 2 eV below and above the absorption edge (5.9600-5.9810 keV and 6.0200-6.0900 keV) and (ii) 0.5 eV in the area around the pre-edge peak and the absorption edge (5.9810-6.0200 keV).

The deconvolution into elemental maps of the FS-XRF data (XANES stack), was performed using the Dynamic Analysis (DA) method implemented in GeoPIXE,[50,51] which allowed separation of the respective contributions of the scatter peaks, the Cr K- and Ba L-lines. This software was also employed to correct for the alignment and drifting of frames in the XANES stack. The TXM-Wizard software,[52] was used to fit the Cr K-edge XANES spectra for regions of interest in the XANES stacks exported from GeoPIXE (each profile obtained by averaging not more than 60 single pixel XANES spectra) and to produce chemical state maps. After definition of the edge jump filter threshold and normalization, since XANES spectra of Cr(VI) compounds present an intense pre-edge peak at 5.993 keV and the absorption edge position shifts about 5 eV toward higher

energies compared to Cr(III)-compounds,[18] Cr-phase maps were obtained by describing the XANES spectra at each pixel as a least squares linear combination (LSLC) of a set of XANES spectra of Cr(VI) and Cr(III) reference compounds. The combination yielding the best fit quality (checked on the basis of the chi-square, reduced chi-square and R-factor values) was chosen as the most likely set of Cr-compounds present at that location.

2.2.2. P06 beamline (DESY). Paint micro-sample F482/8 (from *The Bedroom)* and the aged paint model were investigated by employing a version of the Maia detector (384B) having a better spectral energy resolution (290 eV at Mn-K_α) that was recently installed at the PETRA-III P06 end station. This system already was successfully used for studying complex natural samples.[26,53] It also enables the detection of X-rays at lower energies (down to 2.0 keV rather than 3.3 keV) compared with the Maia-384A model (XFM beamline) (see par. 2.2.1 and Table 1).

During the P06 investigations, a monochromatic primary beam (about $\Delta E/E = 10^{-4}$) in the 5.9-6.0 keV energy range was obtained by means of a Si(111) fixed-exit double-crystal monochromator. KB mirrors were used to focus the beam to a spot size of about 0.7×0.6 μm² (h×v). The position of the sample relative to the beam drifted over a 9 hours period of 4 μm in the horizontal direction and 3 μm in the vertical plane.

By employing dwell times between 1 and 3 ms/pixel, FS-XANES imaging experiments and corresponding data elaboration were performed using the same experimental conditions and software packages as those described above for the XFM experiments (see par. 2.2.1).

2.2.3. ID21 beamline (ESRF). In order to produce a highly monochromatic primary beam (with $\Delta E/E = 10^{-4}$), a Si(220) fixed-exit double-crystal monochromator was employed. The incident beam was focused with Fresnel zone plates down to a size of 0.6×0.2 μm² (h×v) and maintained stable within 0.5 μm vertical and 0.3 μm horizontal across the Cr K-edge (5.96-6.09 keV).

XRF signals were collected in the horizontal plane and at 69° with respect to the incident beam direction by using a single energy-dispersive SDD (Xflash 5100, Bruker with Moxtek thin polymer window). This data acquisition device is characterized by an active area of 80 mm^2, a spectral energy resolution ranging from 150 to 170 eV at 5.9 keV (depending on the electronics configuration), a maximum count rate up to 10^5 per second and sample-solid angle values of the order of a few 10^{-2} sr.[24] Two-dimensional (2D) µ-XRF maps were obtained via raster scanning of the samples using the focused X-ray beam and with dwell times in the 100-300 ms range. Elemental distributions were produced employing the PyMca software,[54] among others to resolve the overlap between the Cr-K and Ba-L lines and the scatter peaks.

To obtain chemical state distributions, the energy of the incoming X-rays was set to two fixed energy values close to the Cr K-edge, where the absorption and consecutively the XRF of particular Cr species are optimal: (i) at 5.993 keV, for favoring the excitation of only the Cr(VI) species, and (ii) at 6.090 keV in order to obtain XRF signals originating from all chromium species. The procedure that was used to produce the Cr chemical state maps is described elsewhere.[18]

Single point µ-XANES spectra were acquired in XRF mode by scanning the primary energy in the 5.96-6.09 keV range and using energy increments of 0.2 eV. For all profiles, the procedure of normalization was performed by means of ATHENA.[55] The same software was also used to carry out a linear combination fitting of the spectra against a library of XANES profiles of Cr-reference compounds. Preliminary tests were performed in order to avoid beam-induced damage of samples.

Regarding sample 224/1 [from *Falling leaves (Les Alyscamps)*] (see par. 3.2.1), a detailed discussion of the Cr-speciation results obtained at ID21 beamline is reported elsewhere.[17] Thus, in what follows, only a selection of these data will be presented and compared with the corresponding ones collected at the XFM beamline.

3. RESULTS AND DISCUSSION

3.1. 2D μ-XRF chromium distributions of original paint micro-samples.

Table 2 summarizes the experimental conditions used for performing SR μ-XRF mapping around

the Cr K-edge of samples 224/1 [from *Falling leaves (Les Alyscamps)*] (Figure 1A) and F482/8

(from *The Bedroom*) (Figure 2A) at the XFM (Maia-384A), P06 (Maia-384B) and ID21 (SDD)

beamlines. The corresponding Cr distributions recorded at 6.09 keV (*i.e.,* above the Cr absorption

edge; a single energy scan is provided as an example) are presented in Figures 1B-C_2 and 2B_1-D_2.

In the following sections, these data sets will be used to describe and compare the technical

features of the different experimental set-ups in terms of acquisition times, radiation doses, spatial

resolution and effects related to their detection geometry.

3.1.1. Acquisition time. As illustrated in Table 2, by using the Maia-384A detector (XFM), the 126

incident E-stack of images around the Cr K-edge (5.96-6.09 keV) of the entire sample 224/1

(610×230 μm^2) took about 300 minutes to record (approximately 2 min. for each energy scan).

Using both versions of the Maia detector, a similar experiment was conducted to scan the entire

area (300×80 μm^2) of sample F482/8; this took around 130 and 210 minutes for the XFM and the

P06 detectors, respectively (*i.e.,* less than 2 min. for each energy scan; see Table 2 for further

details). For both samples, the corresponding Cr total distribution recorded at 6.09 keV is shown in

Figures 1B and 2C-D. The possibility to map the entire sample within a practical time frame (*i.e.,*

taking not more than 5 hours for the acquisition of the entire E-stack of images) allowed a

complete overview of the Cr distribution in these paint samples to be obtained (see section 3.2 for

details).

Figures 1C_1-C_2 and 2B_1-D_2 show a comparison between the total Cr distribution acquired from

equivalent regions of interest of samples 224/1 and F482/8 using the SDD/ID21, Maia-384A/XFM

and Maia-384B/P06 set-ups. According to the values shown in Table 2, for equal dimensions of the

12

scanned areas but different pixel sizes (down to 0.6×0.2 μm^2 for the data sets obtained at ID21), acquisition times of the Maia detector (XFM, P06) are a factor of 10^2-10^3 shorter than those of the SDD (ID21). The result is that during the Maia detector-based experiments, the collection of a stack of 126 maps could be completed in a scanning time that is up to about 10 times shorter than that required to record equivalent maps at only two different energies (*i.e.,* at 5.993 and 6.09 keV) by means of the SDD-based system.

3.1.2. Radiation dose. As a result of the reduced (0.5-3 ms/pixel) dwell time of the Maia detector (XFM, P06), the delivered X-ray dose (expressed as ph/μm^2) per energy scan to the sample is also a factor 10^4-10^2 lower than those of SDD-based investigations at ID21. As Table 2 summarizes, for the experiment conducted at XFM (flux :~1-3$\times10^8$ ph/s), the X-ray dose ranges from 6.3×10^4 ph/μm^2 (dwell time: 0.5 ms) to about 2-5$\times10^5$ ph/μm^2 (1.96 ms dwell time), while they are at around 6×10^6 ph/μm^2 (3 ms dwell time) for those carried out at P06 (flux:~ 9×10^8 ph/s). Regarding the ID21 investigations, depending on both the beam size and dwell times (Table 2 for further details) the dose per energy scan ranges from 1.5×10^7 to 2.3×10^8 ph/μm^2 (flux :~ 2-9$\times10^8$ ph/s). It follows that for the acquisition of an E-stack of 126 maps by means of the Maia detector-based set-ups an X-ray dose of about the same order of magnitude or slightly higher (*i.e.,* not more than a 10 factor) was required with respect to the collection of a set of images at 2 different energy by means of the SDD-based system (Table 2). It is noteworthy to mention that the flux on the samples was reduced with a set of slits or attenuators during the investigations at the three SR end-stations (flux without using attenuators/slits down to about 10^{10}-10^{11} ph/s). Moreover, after investigations, none of the analyzed samples showed any evidence of beam-induced damage under the experimental conditions employed at the three SR facilities.

3.1.3 Spatial resolution and experimental set-up geometry effects. As shown in Figures 1-2, the spatial resolution achieved for the data sets collected using the Maia-384A/XFM (beam size of

approximately 2×2 μm^2) and Maia-384B/P06 (beam size of about 0.6×0.7 μm^2) set-ups do not allow to clearly reveal some features of 5-10 μm dimensions that are on the contrary clearly visible in the corresponding higher-resolution maps acquired by means of the SDD/ID21 microprobe system (beam size down to 0.6×0.2 μm^2). Obviously the lateral resolution is in first place determined by the dimensions of the primary beam and only in second place by the noise level in the resulting elemental/species-specific maps. Regardless of the type of experimental set-ups employed, the recorded Cr distributions are similar within the yellow paint, while the shape and size of the Cr-rich grains localized inside the superficial varnish layer (sample 224/1, Figures $1C_1$-C_2, ROI-1, ROI-2, ROI-3; Figure 5 of ref.[17] to see the corresponding maps collected at ID21) or nearby the surface (sample F482/8, Figure $2B_1$-D_2) are not optimally visualized in the Maia-384A/XFM maps. As Figures $2D_1$-D_2 illustrate, because of the longer dwell time and higher flux used at P06, as well as the increased sensitivity provided by the higher spectral energy resolution of the Maia-384B detector, P06 data does show maps with a slightly improved clarity relative to those obtained at the XFM beamline (Figures $2C_1$-C_2); on the other hand Maia-384B/P06 distributions show a definition lower than would be expected (see Figures $2B_1$-B_2 for a comparison with the equivalent higher resolution ID21 images) due to the fact that maps were recorded using a step size (1×1 μm^2) larger than that of the beam (0.6×0.7 μm^2).

Moreover, changes in the relative positions of Cr-grains can be observed, such as those for example present in Figures $1C_1$-C_2 (*cf.* ROI-1, ROI-2 and ROI-3) and Figures $2B_1$-D_2. The apparent displacement is ascribable to the different geometry of the Maia- and SDD-based experimental set-ups (*cf.* Table 1) and occurs both in the horizontal and vertical direction as a function of the depth of the particles below the paint surface.

Summarizing, as result of the shorter dwell times per pixel (0.5-3 ms), the Maia detector-based microprobe systems allow for scanning of large sample areas with acquisition times and X-ray

doses that are up to 2-3 orders of magnitude lower than those of the SDD-based system. On the other hand, the more limited lateral resolution of the Maia-384A/XFM and Maia-384B/P06 set-ups does not allow resolving fine details at/below the 10 µm level while such details are clearly visible in the maps collected using the SDD/ID21 system.

On the basis of the technical features above-mentioned, in the next section, the Cr-speciation in original paint micro-samples and a photochemically aged chrome yellow paint model sample will be discussed through the comparison between the Cr K-edge FS-XANES imaging results acquired using the Maia-384A/XFM and Maia-384B/P06 set-ups and µ-XRF mapping/single point µ-XANES data obtained by means of the SDD/ID21 microprobe system.

3.2. Cr-speciation in original paint micro-samples and in an aged paint model.

Figures 3-7 show the Cr chemical state maps and XANES spectra obtained from original paint micro-samples 224/1 and F482/8. These data were acquired from the areas shown in Figures 1-2. The results arising from similar investigations of the aged paint model are reported in Figure 8. The relative abundance of Cr-species (expressed as $[Cr(III)]/[Cr_{total}]$) was obtained by LSLC fitting of the XANES spectra and are summarized in Tables S1-S2 of the ESI†.

3.2.1. Sample 224/1 [Falling leaves (Les Alyscamps)]. Figure 3B shows the quantitative Cr-phase maps obtained from the FS-XANES-imaging experiment carried out at XFM. These images were obtained by LSLC fitting of each individual XANES spectrum extracted from the E-stack of images against the XANES profiles of $PbCr_{0.5}S_{0.5}O_4$ (red in Figures 3B-C), $Cr(OH)_3$ (green) and $Cr_2(SO_4)_3 \cdot H_2O$ (blue) as reference compounds. In line with earlier investigations[17] and the XANES spectra of Figures 3D-E (see further), using these components in the fit model yielded the best results. The phase maps illustrate that the lead chromate-based compound is mainly localized in the yellow paint, while Cr(III)-rich particles, present as $Cr_2(SO_4)_3 \cdot H_2O$ and $Cr(OH)_3$ compounds, are

localized both close to the paint/varnish interface and inside the varnish (see also magnified areas

of ROI-1, ROI-2 and ROI-3 in Figure 3C).

The corresponding Cr(III) and Cr(VI) chemical state maps obtained at ID21 (Figure 3A) show a

similar distribution as those of Figure 3B, but at a higher spatial resolution. Inside the varnish,

reduced Cr is often associated with the presence of K and S (Figure $1C_1$; ROI-1 and ROI-2).

In Figures 3D-E (black data points) a selection of the μ-XANES spectra recorded at ID21 (see

ref.[17] for additional data) are compared to the equivalent ones extrapolate from the XANES stack

collected at XFM (*cf.* Figures 3B-C to see the corresponding Cr-phase maps). For each profile

(black data points), the result of the corresponding LSLC fitting (red lines) is also shown (Table S1

of the ESI† for further details).

The XANES spectra obtained from a Cr(III)-particle inside the varnish (Figures 3C-E, ROI-1,

$FL01_{A-ID21/XFM}$) yielded comparable quantitative fitting results, revealing that Cr is present as about

95-97% of Cr(III) (Table S1†); the spectral features mainly resemble to that of a Cr(III)-sulfate

based compound, such as $KCr(SO_4)_2 \cdot 12H_2O$ or $Cr_2(SO_4)_3 \cdot H_2O$ (Figures 3D-E, blue lines). The

data obtained by averaging the single pixel XANES profiles in correspondence of three additional

varnish-embedded micro-grains show similar characteristics, revealing an abundance of

$Cr_2(SO_4)_3 \cdot H_2O$ at around 90% (Figures 3B/4A, $FL01_{B-XFM}$-$FL01_{D-XFM}$ and Table S1†; no

corresponding ID21 profiles available).

In another area inside the surface coating (Figure 3C, ROI-2), a Cr(III)-sulfate based compound

was estimated to be present as well. From the ID21 collected spectrum (Figure 3D, $FL02_{ID21}$), the

relative abundance of this compound was estimated to be around 95%, while a value of around

70% is derived from the corresponding data obtained at XFM (Figure 3E, $FL02_{XFM}$). Close to the

yellow paint surface (Figure 3C, ROI-3), the profiles recorded from another particle resemble that

of $Cr(OH)_3$ (Figure 3D, $FL03_{A-ID21/XFM}$). In this region, the relative amount of Cr(III) is 95% and

88% for the data obtained at ID21 and XFM, respectively (Table S1†). Two micro-grains of similar composition were found to be present in other areas of the varnish, as demonstrated by the corresponding average spectrum (Figure 4A, FL03$_{B-XFM}$-FL03$_{C-XFM}$ and Table S1†; ID21 profiles not available).

Inside the yellow paint underneath the surface (Figure 3C, ROI-2, yellow), the spectral features are more similar to that of the PbCr$_{0.5}$S$_{0.5}$O$_4$ reference compound (Figure 3D-E, yellow$_{ID21/XFM}$). While no evidence of the presence of Cr(III)-species could be observed in the profile recorded at ID21 (Figure 3D, yellow$_{ID21}$), their abundance is at around 20% in the corresponding one obtained at XFM (Figure 3E, yellow$_{XFM}$ and Table S1†).

In different yellow areas of the paint at the interface with the varnish (Figure 4A, FL04$_{XFM}$-FL05$_{XFM}$; ID21 profiles not acquired), the FS-XANES data revealed a relatively high abundance (30-40%) of Cr(III)-compounds [Cr(III)sulfates and/or Cr(OH)$_3$] (see Table S1†). Analysis of a series of Cr K-edge XANES spectra extracted from the stack of images along a single line perpendicular to the exposed surface of the sample (Figure 1B) reveals that the total amount of reduced Cr is at around 20%-35% within the first 10 μm of the cross-section and progressively decreases with depth, reaching values down to 10% inside the yellow bulk of the sample (Figure 4B).

On the basis of the good agreement between the abundances of reduced Cr-species estimated by means of FS-XANES at XFM and those determined on the basis of individual μ-XANES spectra at ID21, we can conclude that FS-XANES imaging investigations provide reliable Cr-speciation results. The different spatial resolution and set-up geometry between the Maia-384/XFM and SDD/ID21 datasets (see Tables 1-2) justify the variance in the fraction of Cr(III) that is observable in some of the XANES data collected from similar areas using the different microprobe systems (*e.g., cf.* FL02$_{XFM}$ /FL02$_{XFM}$; yellow$_{XFM}$/yellow$_{ID21}$). It is important to note that the different angle

of incidence and collection of the beams at ID21 (62° incident angle; 69° collection angle) and

XFM/P06 (normal incidence) mean that different paths are probed into the sample.

By recording spectral data over the entire scanned area, XANES imaging also contributes towards

obtaining a more representative overview of the nature and distribution of different Cr-compounds.

The presence of $Cr(OH)_3$ and Cr(III)-sulfates, present either in the form of small particles at the

varnish/paint interface or as a layer of about 10 μm thickness at the yellow paint surface, strongly

supports the hypothesis that these are products of the degradation process of the original lead

chromate-based pigment.

3.2.2. Sample F482/8 (The Bedroom). The quantitative Cr-phase maps obtained by LSLC fitting

analysis of the XANES stack obtained at the XFM and P06 beamlines are reported in Figures 5A-

B. The XANES profiles of $PbCrO_4$ (red in Figure 5) and $Cr(OH)_3$ (green) were used as component

of the fit. Despite the better spatial and energy resolution of the Maia-384B/P06 microprobe

system, a comparable content of information was obtained from the equivalent data set recorded

using the Maia-384A/XFM setup, in part likely due to the same step sizes (1×1 μm^2) used for

collecting the maps. Notably, $PbCrO_4$ is homogeneously present within the yellow paint, while

$Cr(OH)_3$ is concentrated in a superficial grain and, to a lesser extent, in another region close to the

paint surface (Figures 6B-C and 7B-C; see discussion below about the corresponding quantitative

fit results). In the two latter areas, the chemical speciation maps obtained from the μ-XRF mapping

experiments performed at ID21 (Figure 6A-7A) illustrate a similar distribution of Cr(VI) and

Cr(III)-species at higher spatial resolution.

The single point μ-XANES spectra acquired at ID21 within these areas are shown in Figures 6D-

7D. These profiles are compared to the equivalent ones extrapolated by the XANES stack obtained

at XFM and P06 (Figures 6E-F, 7E-F). Although in some locations the apparent grain displacement

rendered the comparison with the areas analyzed at ID21 less straightforward, the XANES profiles

(black data points in Figures 6-7) show similar spectral features. The corresponding fit (red line) yielded comparable results in terms of $[Cr(III)]/[Cr_{total}]$ ratio, with differences that are within ±10% of each other (see Table S2† for further details).

As shown in Figure 6 (ROI-1), the grain appears to be completely reduced to the Cr(III)-state (about 94-100%); the corresponding XANES spectra strongly resemble that of $Cr(OH)_3$ (Figures 6D-F, B01-02). Profiles collected from other areas adjacent to this particle (B03-05) are more similar to that of $PbCrO_4$ and present an amount of $Cr(OH)_3$ of around 20-35% (Table S2†). In another area at the paint surface (Figure 7, ROI-2), the fit of the XANES spectra (Figures 7D-F, B06-09) yielded a Cr(III)-abundance in the range 25-40% (Table S2†).

The LSLC fitting of a line of single pixel XANES spectra (Figure 5C), obtained from a line perpendicular to the exposed surface of the sample (Figures 5A-B) shows that the relative abundance of $Cr(OH)_3$ is around 25% along the first 7-8 µm of the cross-section; this value progressively decreases with depth, reaching values down to 5% inside the yellow bulk of the sample. In addition, the fit yielded comparable results for both the XFM and P06 data sets.

On the basis of these investigations, the presence of $Cr(OH)_3$ both in the form of particles near the paint surface and as a layer of about 7-8 µm thickness in the upper part of the yellow paint suggests that this compound is the product of the degradation process of the original lead chromate pigment. Considering that in this and some of the other samples that were examined (see par. 3.2.1 and ref. [17]), this compound shows a similar distribution, we do not assume it was originally present [for example in the form of viridian $(Cr_2O_3 \cdot 2H_2O)$, a pigment also frequently employed by Van Gogh].[56,57]

In the following section, the results obtained from original paint-micro samples will be complemented by comparing Cr K-edge FS-XANES imaging and single point µ-XANES data collected from an artificially aged chrome yellow paint model.

3.2.3. Artificially aged chrome yellow paint model. Figures 8A-B show a photograph of the S_{3D} ($PbCr_{0.2}S_{0.8}O_4$) paint model before and after photochemical aging and a photomicrograph of a thin section obtained from the aged sample. As described elsewhere,[19] after light exposure, this material becomes darker, due to the formation of a brown alteration layer at the exposed surface (Figure 8B). In view of the limited thickness (about 4-5 μm) of this layer, the Maia-384B/P06 microprobe was used to record a high definition Cr K-edge FS-XANES image set at ~0.6 μm spatial resolution. In Figures 8C-D the area investigated and the resulting quantitative Cr-phase maps are shown. Consistent with earlier investigations[19] and with the single point μ-XANES spectra collected at ID21 along a line from the exposed surface of the paint (Figure 8E), the best LSLC fitting result was obtained by including the XANES profiles of $PbCr_{0.2}S_{0.8}O_4$ (red in Figure 8D), $Cr(OH)_3$ (green) and Cr(III) acetylacetonate [$Cr(C_5H_7O_2)_3$] (blue) in the fitting model. As Figure 8 D shows, the latter two compounds appear localized in the superficial brown alteration layer, while the lead chromate-based compound is the main constituent of the yellow paint underneath.

The LSLC fitting of a line of XANES spectra obtained perpendicularly to the exposed surface of the sample (Figure 8C) yields a similar [Cr(III)]/[Cr_{total}] ratio profile for the data obtained both at P06 and ID21 (Figures 8F-G). The fraction of Cr(III) progressively decreases from the superficial brown layer (about 40-50% within the upper 4-5 μm) toward the yellow bulk of the sample (approximately 5%). Despite differences in the absolute percentage of $Cr(OH)_3$ and $Cr(C_5H_7O_2)_3$ that result from the analysis (*e.g.,* for the "top" spectra collected at ID21 and P06 the percentage relative amount of $Cr(C_5H_7O_2)_3$ was around 16% and 7%, respectively, while those of $Cr(OH)_3$ were about 36% and 40% ; *cf.* Figures 8F-G), a recurring observation is that the latter compound only seems to be present at the very surface (top 2-3 μm).

4. CONCLUSIONS

In this work, synchrotron radiation-based full spectral (FS)-XANES imaging in XRF mode using both the Maia-384A (at the XFM beamline, Australian Synchrotron) and the Maia-384B detection systems (operational at the P06 X-ray micro/nanoprobe endstation, PETRA-III, DESY) was successfully used for studying the nature and distribution of secondary Cr-compounds of lead chromate-based pigments (chrome yellows) and quantitatively determining their abundance in two paint micro-samples taken from artworks by Vincent van Gogh and in an artificially aged paint model. A comparison with complementary Cr K-edge μ-XRF mapping/single point μ-XANES investigations using a more conventional silicon drift detector (SDD) (operational at the ID21 microscope, ESRF), allowed us to conclude as follows:

i) From a technical point of view, the XRF scanning times and the delivered X-ray doses to samples using the Maia detector could be reduced with 2-3 orders of magnitude relative to similar experiments conducted by means of a SDD. The lower spectral energy resolution of the Maia detector (290 and 375eV) with respect to the SDD (ranging from 150 to 170 eV) did not turn out to be a limiting factor, even in the case of Ba L-lines overlapping with Cr K-lines. On the other hand, the worst spatial resolution of the Maia 384-based beamlines did not allow to reveal at the same level of definition details of dimensions 5-10 μm that on the other hand are clearly visible in the corresponding high-resolution maps collected using the SDD/ID21 microprobe system. However, the improved spatial and energy resolution of the Maia-384B/P06 microprobe system (~0.6 μm) with respect to that of the Maia-384A/XFM set-up (~2 μm) were successfully exploited for characterizing the composition of the superficial micrometric Cr(III)-rich alteration layer of a photochemical aged $PbCr_{0.2}S_{0.8}O_4$ paint.

ii) Through the investigations of larger areas of the sample and the extraction of XANES profiles from all locations in the examined region, Maia-XANES imaging contributed in deepening

knowledge on the nature and distribution of secondary Cr-compounds relative to μ-XRF mapping/single point μ-XANES investigations of a selection of smaller regions of interest. In all the original paint micro-samples investigated here, the widespread distribution at the paint surface of Cr(III)-compounds [*i.e.,* Cr(III)-sulfates and Cr(OH)$_3$] in forms of both micro-grains and micrometric layers (about 8-10 μm in thickness) strongly supports the hypothesis that they were not originally present but are products of the degradation of the original pigment.

iii) With the exception of a few cases in which differences in the amount of Cr(III) could be ascribed to a difference in the spatial resolution and experimental set-up geometry of the microprobe systems employed, the comparable quantitative Cr-speciation results obtained by comparing the FS-XANES imaging and single point μ-XANES data prove that the former technique may be used as a reliable method for quantitatively determining the abundance of different Cr-species.

On the basis of this study, the use of large area FS-XANES mapping using the Maia detector as complementary tool to high-spatial and spectral energy resolution μ-XRF mapping/single point μ-XANES measurements using more traditional ED-XRF detectors open up the possibility to extend this methodological approach also to the investigation of the alteration process of other pigments.

Alternative data collection strategies relevant to explore are full-field XANES imaging (*i.e.,* not involving sample scanning) in transmission and in fluorescence mode. The former mode of operation is currently present at Stanford Synchrotron Radiation Lightsource[58] and at ID21,[59] and has found only a few applications in the field of cultural heritage, such as model paints[59] and ceramics;[60] the latter was recently implemented at BM26 of ESRF and successfully employed for the investigation of soils.[61]
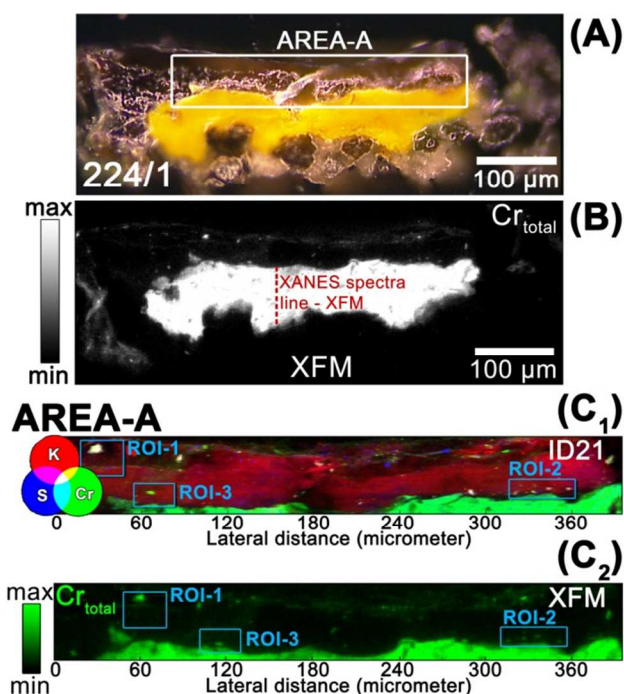
Figure 1. Sample 224/1–*Falling leaves (Les Alyscamps)*. (A) Photomicrograph and (B) μ-XRF Cr_{total} distribution (6.09 keV) of the entire sample collected following completion of the XRF mode-XANES imaging at the XFM beamline (Maia-384A detector). RGB μ-XRF distribution of (C$_1$) K/Cr_{total}/S and (C$_2$) Cr_{total} acquired at the ID21 [silicon drift detector (SDD)] and XFM beamlines, respectively (see Table 2 for experimental details). Maps of (C$_1$-C$_2$) were acquired in the area shown by the white rectangle in (A). In (C$_1$-C$_2$), cyan rectangles indicate the regions were XANES spectra were recorded (see Figure 3D-E). In (B), the red dotted line illustrates the position where a line of Cr K-edge XANES spectra was extracted from the E-stack of images (see Figure 4B).
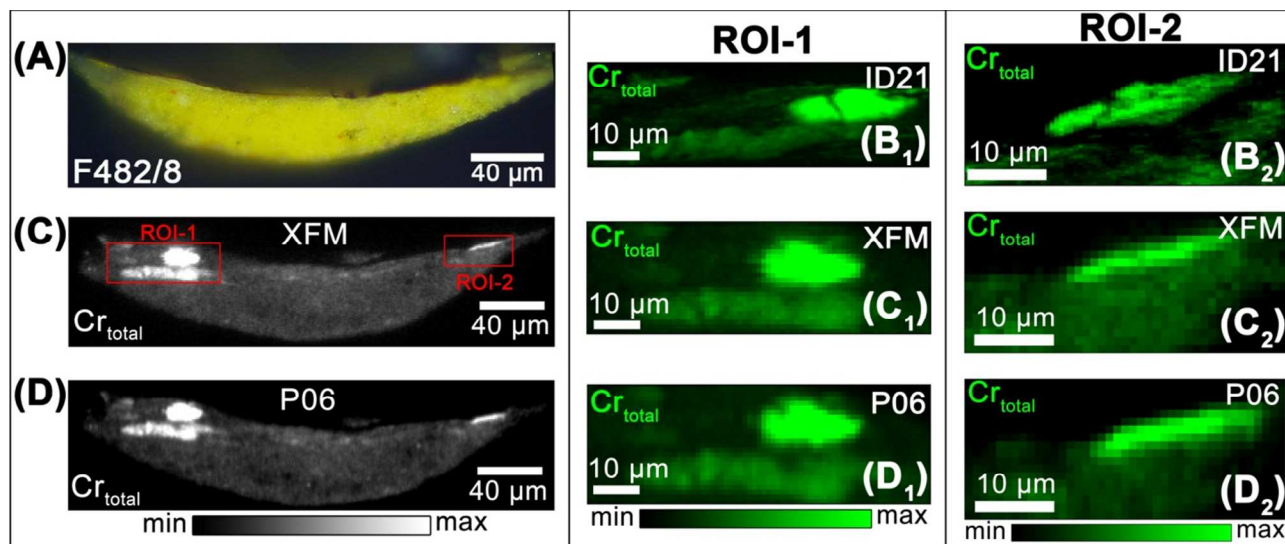
Figure 2. Sample F482/8–*The Bedroom*. (A) Photomicrograph and μ-XRF Cr$_{total}$ distribution (6.09 keV) obtained at the beamlines (B$_1$-B$_2$) ID21 (SDD), (C) XMF (Maia-384A detector) and (D) P06 (Maia-384B detector). (C$_1$-D$_2$) Magnified maps of ROI-1 and ROI-2 obtained from (C) and (D) (see Table 2 for experimental details).
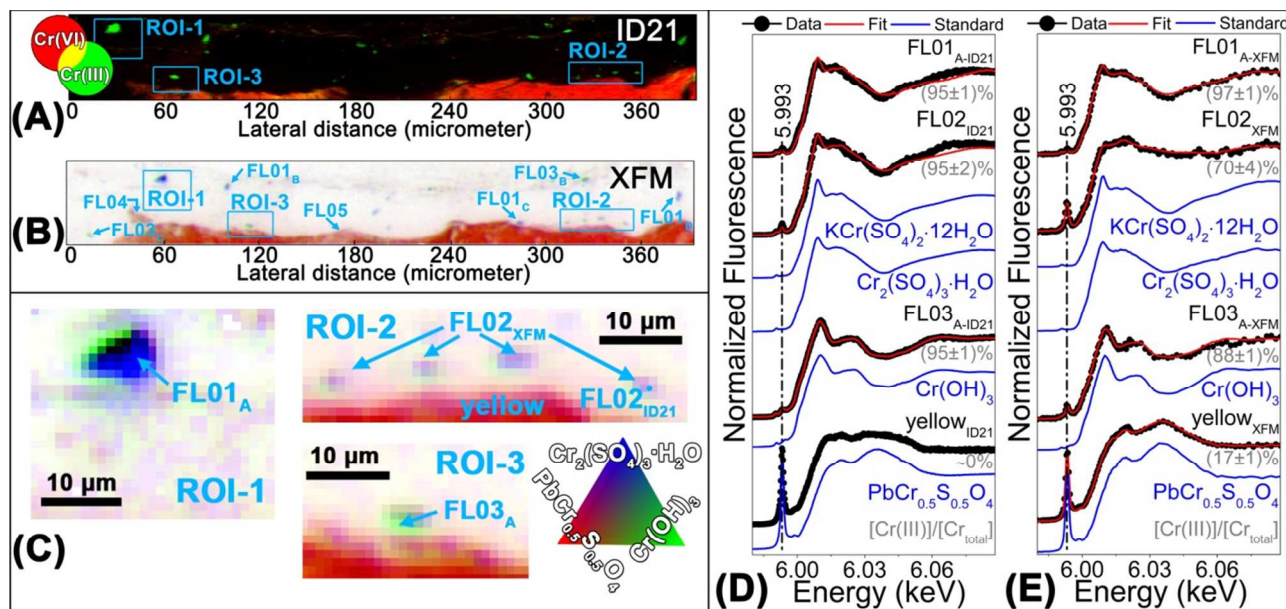
Figure 3. Cr-speciation results of 224/1. (A) Cr(VI)/Cr(III) chemical state maps acquired at ID21 (see Figure 1C$_1$). (B) Quantitative Cr-phase maps and (C) corresponding magnification of the regions of interest (see also ref. [17] for further details) obtained from the linear combination fitting of the XANES stack collected at the beamline XFM using the profiles of PbCr$_{0.5}$S$_{0.5}$O$_4$ (red), Cr(OH)$_3$ (green) and Cr$_2$(SO$_4$)$_3$·H$_2$O (blue) as reference compounds (see Figure 1C$_2$). RG result of the fit (red) of the XANES profiles by linear combination of PbCr$_{0.5}$S$_{0.5}$O$_4$, Cr(OH)$_3$ and Cr$_2$(SO$_4$)$_3$·H$_2$O (blue) to the spectra (black) obtained at (D) ID21 [beam size (v×h): 0.23×0.74 μm^2; dose: ~3.5×10^{12} ph/μm^2] and (E) XFM (number of averaged pixels: 3-30; pixel sizes: 1×1 μm^2; dose:~7×10^7 ph/μm^2). Measurements positions are shown in (B-C) by cyan arrows and labels. In (D-E), grey labels show the percentage relative amount of Cr(III) (Table S1 of ESI † for details).
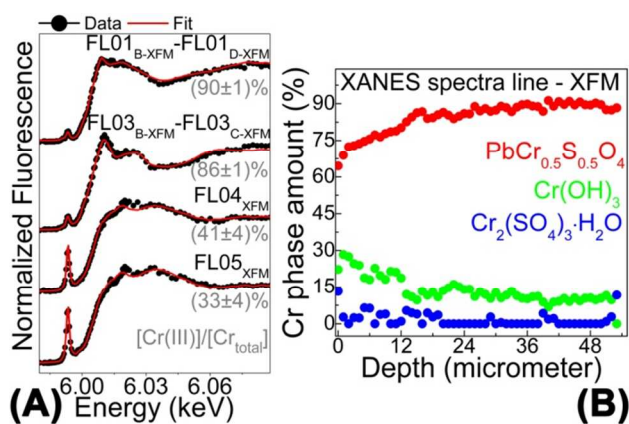
Figure 4. Additional Cr K-edge full spectral-XANES data extracted from 224/1. (A) Profiles (black) (number of averaged pixels: 20-30; pixel sizes: 1×1 μm^2; dose:$\sim7\times10^7$ ph/μm^2) and corresponding result of the linear combination fitting (red) of $PbCr_{0.5}S_{0.5}O_4$, $Cr(OH)_3$ and $Cr_2(SO_4)_3\cdot H_2O$ as reference compounds (see Figure 3A and Table S1†). (B) Percentage relative amount of different Cr-phases *vs.* the depth obtained by linear combination fitting of the single pixel XANES spectra extracted from the region of the images stack shown in Figure 1B.

Figure 5. Cr-speciation results of F482/8. Quantitative Cr-phase maps obtained from the linear combination fit of the Cr K-edge XANES stack collected at (A) XFM and (B) P06 using the profiles of PbCrO$_4$ (red) and Cr(OH)$_3$ (green) as reference compounds (see Figures 2C-D). (C) Percentage relative amount of PbCrO$_4$ (red) and Cr(OH)$_3$ *vs.* the depth obtained by linear combination fitting of the single pixel XANES spectra extrapolated from the region shown in (A) (circles) and (B) (triangles).
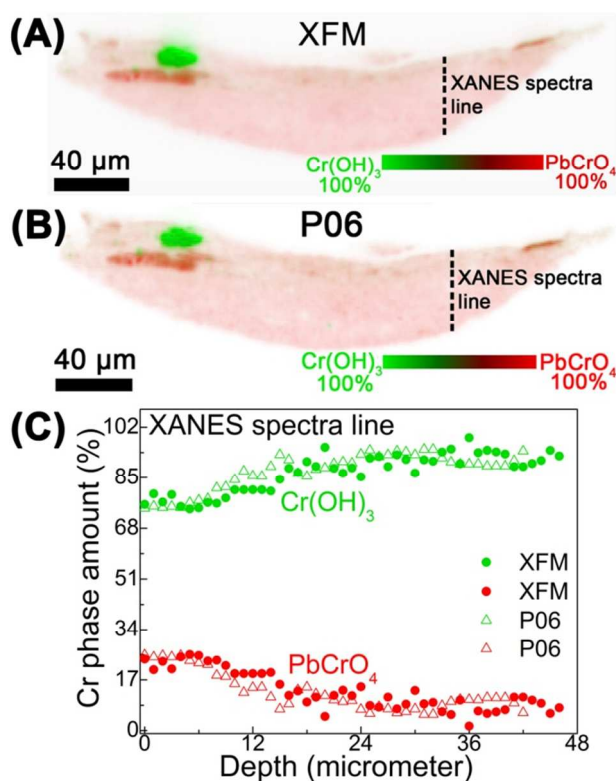
Figure 6. Cr-speciation results of F482/8: ROI-1. (A) RG Cr(VI)/Cr(III) chemical state maps collected at ID21 and (B) quantitative Cr-phase maps obtained from the linear combination fitting of the Cr K-edge XANES stack acquired at (B) XFM and (C) P06 using the profiles of $PbCrO_4$ (red) and $Cr(OH)_3$ (green) as reference compounds (see Figures $2C_1,D_1$). Result of the fit (red) of the XANES profiles by linear combination of $PbCrO_4$ and $Cr(OH)_3$ (blue) to the spectra (black) collected at (D) ID21 [beam size (v×h): 0.2×0.6 μm^2; dose: ~$4×10^{11}$-$2×10^{12}$ ph/μm^2], (E) XFM and (F) P06 (number of averaged pixels: 3-11; pixel sizes: 1×1 μm^2; $dose_{XFM}$:~$2.6×10^7$ ph/μm^2; $dose_{p06}$: ~$8×10^8$ ph/μm^2). Measurement positions are shown in (A-C) by arrows and labels. In (D-F) grey labels show the percentage relative amount of Cr(III) (Table S2† for details).
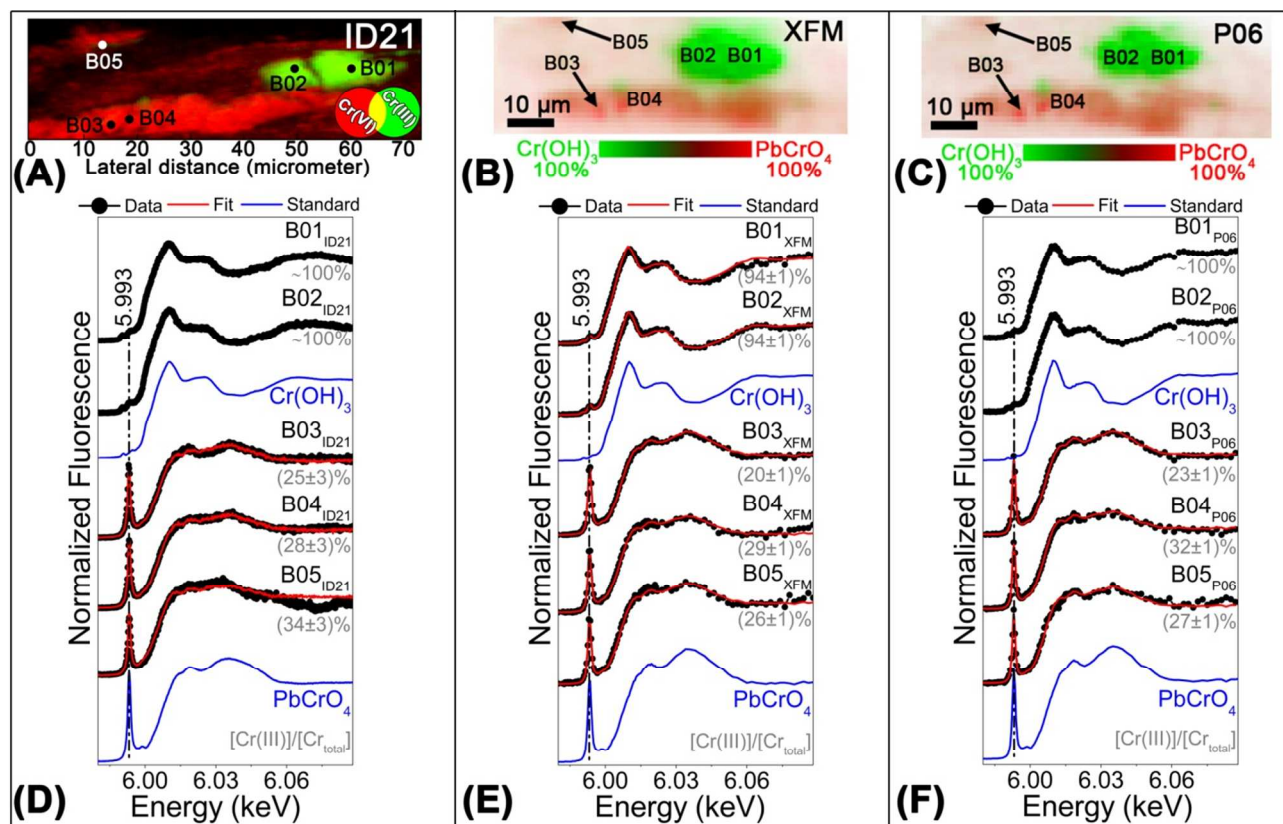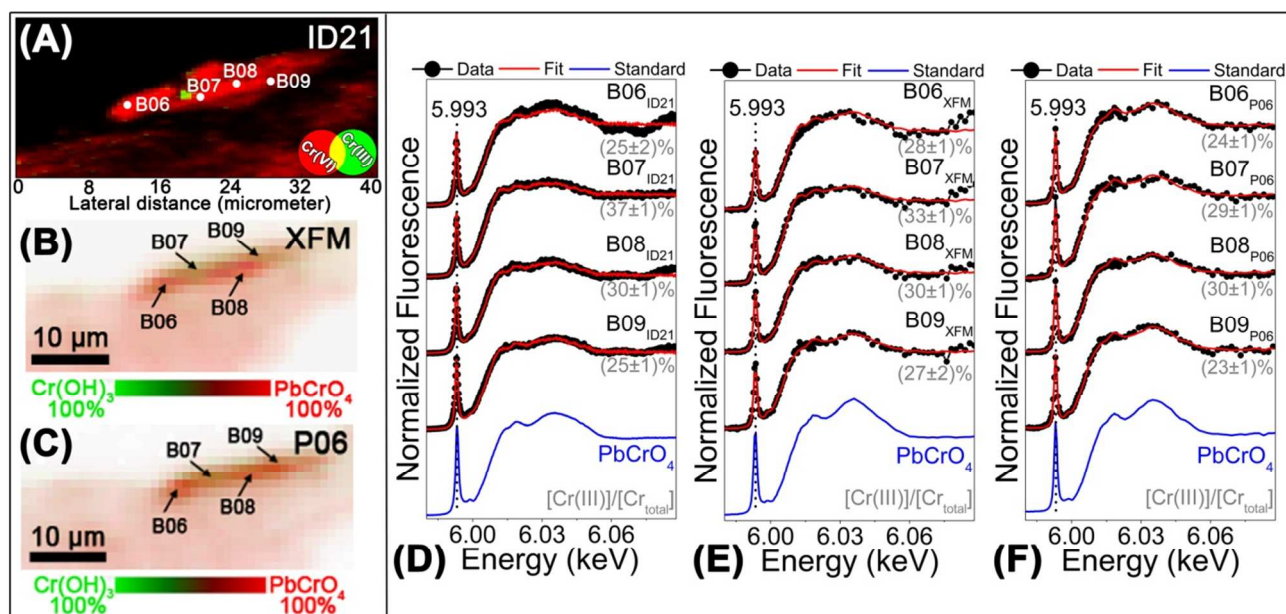
Figure 7. Cr-speciation results of F482/8: ROI-2. (A) RG Cr(VI)/Cr(III) chemical state maps obtained at ID21 and (B) quantitative Cr-phase maps obtained from the linear combination fit of the Cr K-edge XANES stack collected at (B) XFM and (C) P06 using the profiles of $PbCrO_4$ (red) and $Cr(OH)_3$ (green) as reference compounds (see Figures $2C_2,D_2$). Result of the fit (red) of the XANES profiles by linear combination of $PbCrO_4$ and $Cr(OH)_3$ (blue) to the spectra (black) collected at (D) ID21 [beam size (v×h): 0.2×0.6 μm^2; dose: ~ 1.4×10^{12} ph/μm^2], (E) XFM and (F) P06 (number of averaged pixels: 3-6; pixel sizes: 1×1 μm^2; dose$_{XFM}$: ~2.6×10^7 ph/μm^2; dose$_{P06}$: ~8×10^8 ph/μm^2). Measurement positions are shown in (A-C) by black arrows and labels. In (D-F) grey labels show the percentage relative amount of Cr(III) (Table S2† for details).
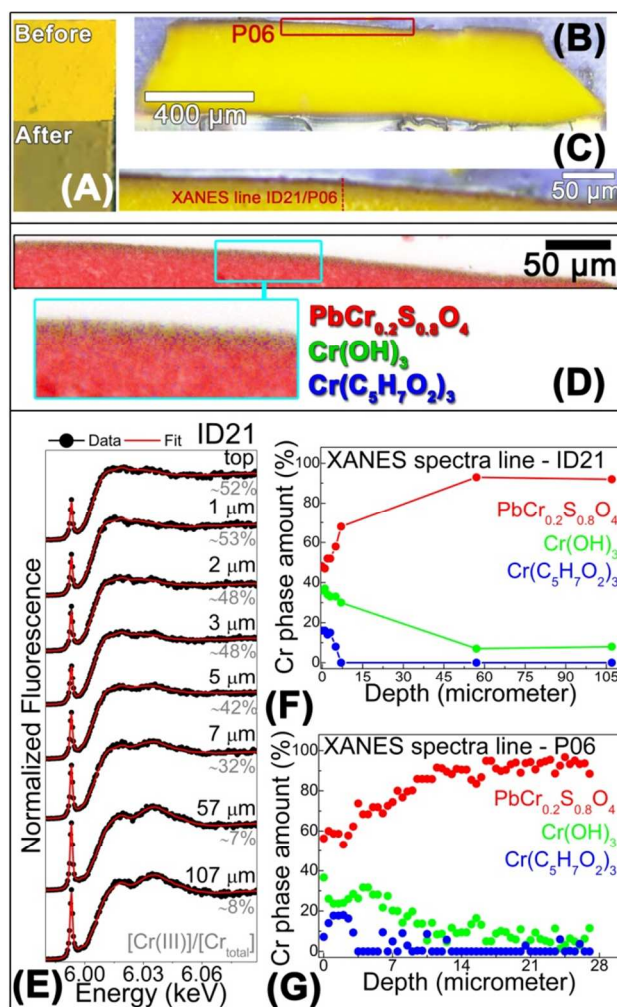
Figure 8. (A) Photograph (top) before and (bottom) after light exposure and (B) photomicrograph of a thin section obtained from the aged $PbCr_{0.2}S_{0.8}O_4$ oil paint model. (C) Magnification of the area where the Maia 384B/P06 XANES imaging analysis was performed and (D) corresponding quantitative Cr-phase maps obtained from the linear combination fitting of $PbCr_{0.2}S_{0.8}O_4$ (red), $Cr(OH)_3$ (green) and $Cr(C_5H_7O_2)_3$ (blue) of the Cr K-edge XANES stack (pixel sizes: 0.5×0.5 μm^2; map sizes: 460×40 μm^2; dwell time: 1 ms; dose: $\sim1.3\times10^6$ ph/μm^2; acquisition time: ~30 min.). (E) Result of the fit (red) by linear combination of $PbCr_{0.2}S_{0.8}O_4$, $Cr(OH)_3$ and $Cr(C_5H_7O_2)_3$ to the spectra (black) obtained at ID21 [beam size (v×h): 0.25×0.6 μm^2; dose:$\sim6\times10^{11}$ ph/μm^2] and corresponding (F) percentage relative amount *vs.* the depth. (G) Equivalent results to those of (F) obtained by linear combination fitting of the single pixel XANES spectra of the images stack collected at P06. The acquisition region of these profiles is shown in (C).

Table 1. Experimental set-up conditions used for performing Cr-speciation investigations (5.96-6.09 keV energy spectral range) at the beamlines XFM (AS, Melbourne, AUS), P06 (DESY, Hamburg, DE) and ID21 (ESRF, Grenoble, FR).

Beamline (SR facility)	Focusing optics	Beam size (h×v) (μm^2)	Change of the beam position during a scan (h×v) (μm^2)	Detector	Active area /solid angle	Geometry	Energy resolution at 6 keV (eV)	Dwell time (ms/pixel)	Photon flux (ph/s)[g]
XFM (AS)	KB mirrors	2×2	~3×3[b]	Maia 384A	384 mm^2/ ~1.3 sr	180°-Backscattering	375	0.5-2	~1-3×10^8
P06 (DESY)[a]	KB mirrors	0.7×0.6	~4×3[b]	Maia 384B	384 mm^2/ ~1.3 sr	180°-Backscattering	290	0.5-3[e]	~4×10^6; 9×10^8
ID21 (ESRF)[a]	Fresnel zone plates	down to 0.6×0.2	~0.3×0.5[d]	Silicon drift diode (Xflash 5100, Bruker)	80 mm^2/ few 10^{-2} sr	Incident angle: 62° Detection angle: 69°	150-170	100-300[f]	~2-9×10^8

[a] Measurements carried out during 2 different experiments (see Table 2 for additional details).
The change of the beam position was measured: [b] over a 24 hours period; [c] over a 9 hours period; [d] as a function of the energy.
Typical range values are: [e] 0.5-50 ms/pixel; [f] 0.1-2 s/pixel.
[g] Values obtained using attenuators/slits. Maximum flux of about 10^{10}-10^{11} ph/s.

1
2
3
4
5
6
7
8
9
10
11
12
13
...

Table 2. Comparison among the experimental conditions employed for the acquisition of the XRF maps of original paint-micro samples at the beamlines XFM (AS), P06 (DESY) and ID21 (ESRF).

Sample	Maps	Map size (h×v) (μ^2)	Pixel size (h×v) (μm^2)	Pixel total number	Dwell time (ms/pixel)	Acquisition time per energy scan (min:s)	Acquisition time (min)[a]	Absolute photon flux (ph/s)	Dose per energy scan (ph/μm^2)	Dose (ph/μm^2)[a]
224/1 *Falling leaves (Les Alyscamps)*	Entire sample$_{XFM}$ (Figure 1B)	610×230	1×1	$1.403×10^5$	0.49	2:23	300	$1.3×10^8$	~$6.3×10^4$	~$8×10^6$
	AREA-A$_{XFM}$ (Figure 1C$_1$)	395×53	1×1	$2.0935×10^4$	1.96	1:12	150	$2.7×10^8$	~$5.3×10^5$	~$6.7×10^7$
	AREA-A$_{ID21}$ (Figure 1C$_2$)	395×54	1×0.5[c]	$4.266×10^4$	150	110:00	215	$9.2×10^8$	~$2.3×10^8$	~$4.6×10^8$
F482/8 *The Bedroom*	Entire sample$_{XFM}$ (Figure 2C)	300×80	1×1	$2.4×10^4$	0.99	1:00	130	$2.1×10^8$	~$2×10^5$	~$2.6×10^7$
	Entire sample$_{P06}$ (Figure 2D)	300×80	1×1	$2.4×10^4$	3	1:40	210	$9×10^8$	~$6.4×10^6$	~$8×10^8$
	ROI-1$_{XFM}$[b] (Figure 2C$_1$)	73×24	1×1	$1.752×10^3$	0.99	0:04	10	$2.1×10^8$	~$2×10^5$	~$2.6×10^7$
	ROI-1$_{P06}$[b] (Figure 2D$_1$)	73×24	1×1	$1.752×10^3$	3	0:07	15	$9×10^8$	~$6.4×10^6$	~$8×10^8$
	ROI-1$_{ID21}$ (Figure 2B$_1$)	73.8×22.6	0.6×0.2[d]	$1.3899×10^4$	150[e] 300[f]	36:00 72:00	108	$1.7×10^8$	~$1.5×10^7$ ~$1.8×10^7$	~$3.3×10^7$
	ROI-2$_{XFM}$[b] (Figure 2C$_2$)	41×18	1×1	$7.38×10^2$	0.99	0:02	4	$2.1×10^8$	~$2×10^5$	~$2.6×10^7$
	ROI-2$_{P06}$[b] (Figure 2D$_2$)	41×18	1×1	$7.38×10^2$	3	0:03	6-7	$9×10^8$	~$6.4×10^6$	~$8×10^8$
	ROI-2$_{ID21}$ (Figure 2B$_2$)	40.8×18	0.6×0.2[d]	$6.12×10^3$	150[e] 300[f]	17:00 33:00	50	$1.7×10^8$	~$3×10^7$ ~$5×10^7$	~$8×10^7$

[a] Values refer to the acquisition of 126 XRF images for the measurements performed at XFM and P06 beamlines, while to that of 2 images for the analysis carried out at ID21.
[b] Magnified area selected from the larger map collected from the entire sample.
Beam sizes (h×v) of: [c] 0.74×0.23 μm^2; [d] 0.6×0.2 μm^2.
[e] at 6.09 keV.
[f] at 5.993 keV.

NOTES AND REFERENCES

[1] L. Bertrand, L. Robinet, M. Thoury, K. Janssens, S. X. Cohen, S. Schöder, *Appl. Phys. A: Mater. Sci. Process.,* 2012, **106**, 377-396.

[2] K. Janssens, M. Alfeld, G. Van der Snickt, W. De Nolf, F. Vanmeert, M. Radepont, L. Monico, J. Dik, M. Cotte, G. Falkenberg, C. Miliani, B. G. Brunetti, *Annu. Rev. Anal. Chem.*, 2013, **6**, 399-425.

[3] M. Cotte, J. Susini, J. Dik, K. Janssens, *Acc. Chem. Res.*, 2010, **43,** 705-714.

[4] M. Radepont, W. De Nolf, K. Janssens, G. Van der Snickt, Y. Coquinot, L. Klaassen, M. Cotte, J. Susini, N. Metrich, A. Moscato, C. Gratziu, A. Bertagnini, M. Pagano, *Anal. Atom. Spectrom.*, 2011, **26**, 959-968*Chem. (Washington, DC, U. S.),* 2006, **78**, 7484-7492.

[5] M. Radepont, W. De Nolf, K. Janssens, G. Van der Snickt, Y. Coquinot, L. Klaassen, M. Cotte, *J. Anal. Atom. Spectrom.*, 2011, **26**, 959-968.

[6] L. Robinet, M. Spring, S. Pagès-Camagna, D. Vantelon, N. Trcera, *Anal. Chem. (Washington, DC, U. S.),* 2011, **83,** 5145-5152

[7] I. Cianchetta, I. Colantoni, F. Talarico, F. D'Acapito, A. Trapananti, C. Maurizio, S. Fantacci, I. Davoli, *J. Anal. Atom. Spectrom.*, 2012, **27,** 1941-1948.

[8] L. Samain, F. Grandjean, G. J. Long, P. Martinetto, P. Bordet, J. Sanyova, D. Strivay, *J. Synchrotron Radiat.,* 2013, **20,** 460-473.

[9] L. Samain, G. Silversmit, J. Sanyova, B. Vekemans, H. Salomon, B. Gilbert, F. Grandjean, G. J. Long, R. P. Hermann, L. Vincze, D. Strivay, *J. Anal. Atom. Spectrom.,* 2011, **26,** 930-941.

[10] L. Cartechini, C. Miliani, B. G. Brunetti, A. Sgamellotti, C. Altavilla, E. Ciliberto, F. D'Acapito, *Appl. Phys. A: Mater. Sci. Process.*, 2008, **92**, 243-250.

[11] C. Santoro, K. Zarkout, A. Le Ho, F. Mirambet, D. Gourier, L. Binet, S. Pagès-Camagna, S. Reguer, S. Mirabaud, Y. Le Du, P. Griesmar, N. Lubin-Germain, M. Menu, *Appl. Phys. A: Mater. Sci. Process.,* 2014, **114,** 637-645.

[12] G. Van der Snickt, J. Dik, M. Cotte, K. Janssens, J. Jaroszewicz, W. De Nolf, J. Groenewegen, L. van der Loeff, *Anal. Chem. (Washington, DC, U. S.),* 2009, **81**, 2600-2610.

[13] G. Van der Snickt, K. Janssens, J. Dik, W. De Nolf, F. Vanmeert, J. Jaroszewicz, M. Cotte, G. Falkenberg, L. van der Loeff, *Anal. Chem. (Washington, DC, U. S.),* 2012, **84**, 10221-10228.

[14] J. L. Mass, R. Opila, B. Buckley, M. Cotte, J. Church, A. Mehta, *Appl. Phys. A: Mater. Sci. Process.,* 2013, **111,** 59-68.

[15] L. Zanella, F. Casadio, K. A. Gray, R. Warta, Q. Ma, J. F. Gaillard, *J. Anal. Atom. Spectrom.*, 2011, **26**, 1090-1097.

[16] L. Monico, G. Van der Snickt, K. Janssens, W. De Nolf, C. Miliani, J. Dik, M. Radepont, E. Hendriks, M. Geldof, M. Cotte, *Anal. Chem. (Washington, DC, U. S.),* 2011, **83**, 1224-1231.

[17] L. Monico, K. Janssens, F. Vanmeert, M. Cotte, B. G. Brunetti, G. Van der Snickt, M. Leeuwestein, J. Salvant Plisson, M. Menu, C. Miliani, *Anal. Chem. (Washington, DC, U.S.),* 2014, **86**, 10804–10811.

[18] L. Monico, G. Van der Snickt, K. Janssens, W. De Nolf, C. Miliani, J. Verbeeck, H. Tian, H. Tan, J. Dik, M. Radepont, M. Cotte, *Anal. Chem. (Washington, DC, U. S.)*, 2011, **83**, 1214-1223.

[19] L. Monico, K. Janssens, C. Miliani, G. Van der Snickt, B. G. Brunetti, M. Cestelli Guidi, M. Radepont, M. Cotte, *Anal. Chem. (Washington, DC, U. S.)*, 2013, **85**, 860-867.

[20] C. Strohm, F. Perrin, M. C. Dominguez, J. Headspith, P. Linden, O. Mathon, *J. Synchrotron Radiat.,* 2011, **18**, 224-228.

[21] A. J. Dent, G. Cibin, S. Ramos, S. A. Parry, D. Gianolio, A. D. Smith, P. E. Robbins, *J. Phys.: Conf. Ser.,* 2013, **430**, 012023.

[22] P. Lechner, A. Pahlke, H. Soltau, *X-Ray Spectrom.*, 2004, **33**, 256-261.

[23] P. Sangsingkeow, K. D. Berry, E. J. Dumas, T. W. Raudorf, T. A. Underwood, *Nucl. Instrum. Methods Phys. Res., Sect. A*, 2003, **505,** 183-186.

[24] M. Cotte, J. Szlachetko, S. Lahlil, M. Salomé, V. A. Solé, I. Biron, J. Susini, *J. Anal. Atom. Spectrom.*, 2011, **26**, 1051-1059.

[25] L. Bertrand, S. Schoeder, D. Anglos, M. Breese, K. Janssens, M. Moini, A. Simon, "Mitigation strategies for radiation damage in the analysis of ancient materials", *Trends Anal. Chem.*, 2014, in press.

[26] C. G. Ryan, D. P. Siddons, R. Kirkham, Z. Y. Li, M. D. de Jonge, D. J. Paterson, A. Kuczewski, D. L. Howard, P. A. Dunn, G. Falkenberg, U. Boesenberg, G. De Geronimo, L. A. Fisher, A. Halfpenny, M. J. Lintern, E. Lombi, K. A. Dyl, M. Jensen, G. F. Moorhead, J. S. Cleverley, R. M. Hough, B. Godel, S. J. Barnes, S. A. James, K. M. Spiers, M. Alfeld, G. Wellenreuther, Z. Vukmanovic, S. Borg, *J. Phys.: Conf. Ser.* 2014, **499**, 012002.

[27] D. P. Siddons, R. Kirkham, C. G. Ryan, G. De Geronimo, A. Dragone, A. J. Kuczewski, Z. Y. Li, G. A. Carini, D. Pinelli, R. Beuttenmuller, D. Elliott, M. Pfeffer, T. A. Tyson, G. F. Moorhead, P. A. Dunn, *J. Phys.: Conf. Ser.* 2014, **499**, 012001.

28 C. G. Ryan, R. Kirkham, R. M. Hough, G. Moorhead, D. P. Siddons, M. D. de Jonge, D. J. Paterson, G. De Geronimo, D. L. Howard, J. S. Cleverley, *Nucl. Instrum. Methods Phys. Res., Sect. A,* 2010, **619**, 37-43.

29 C. G. Ryan, *Int. J. Imag. Syst. Tech.,* 2000, **11**, 219−230.

30 E. Lombi, M. D. de Jonge, E. Donner, C. G. Ryan, D. Paterson, *Anal. Bioanal. Chem.,* 2011, **400**, 1637−1644.

31 E. Donner, D. L. Howard, M. D. de Jonge, D. Paterson, M. H. Cheah, R. Naidu, E. Lombi, *Environ. Sci. Technol.,* 2011, **45**, 7249−7257.

32 P. Wang, N. W. Menzies, E. Lombi, B. A. McKenna, M. D. de Jonge, E. Donner, F. P. C. Blamey, C. G. Ryan, D. J. Paterson, D. L. Howard, S. A. James, P. M. Kopittke, *Sci. Total Environ.*, 2013, **463**, 131-139.

33 M. Lintern, R. Anand, C. G. Ryan, D. Paterson, *Nat. Commun.,* 2013, **4,** DOI: 10.1038/ncomms3614.

34 S. A. James, D. E. Myers, M. D. de Jonge, S. Vogt, C. G. Ryan, B. A. Sexton, P. Hoobin, D. Paterson, D. L. Howard, S. C. Mayo, M. Altissimo, G. F. Moorhead, S. W. Wilkins, *Anal. Bioanal. Chem.,* 2011, **401,** 853−864.

35 E. Lombi, E. Smith, T. H. Hansen, D. Paterson, M. D. de Jonge, D. L. Howard, D. P. Persson, S. Husted, C. G. Ryan, J. K. Schjoerring, *J. Exp. Bot*, 2011, **62,** 273-282.

36 J. Z. Zhang, N. S. Bryce, R. Siegele, E. A. Carter, D. Paterson, M. D. de Jonge, D. L. Howard, C. G. Ryan, T. W. Hambley, *Integr. Biol*., 2012, **4,** 1072-1080.

37 Liu, Tianqing, I. Kempson, M. D. de Jonge, D. L. Howard, B. Thierry, *Nanoscale*, 2014, **6**, 9774−9782.

38 D. L. Howard, M. D. de Jonge, D. Lau, D. Hay, M. Varcoe-Cocks, C. G. Ryan, R. Kirkham, G. F. Moorhead, D. Paterson, D. Thurrowgood, *Anal. Chem. (Washington, DC, U. S.),* 2012, **84**, 3278−3286.

39 E. Lombi, M. D. de Jonge, E. Donner, P. M. Kopittke, D. L. Howard, R. Kirkham, C. G. Ryan, D. Paterson, *PLoS ONE*, 2011, **6**, DOI:10.1371/journal.pone.0020626.

40 P. M. Kopittke, M. D. de Jonge, N. W. Menzies, P. Wang, E. Donner, B. A. McKenna, D. Paterson, D. L. Howard, E. Lombi, *Plant Physiol.*, 2012, **159**, 1149-1158.

41 A. Carey, E. Lombi, E. Donner, M. D. de Jonge, T. Punshon, B. P. Jackson, M. L. Guerinot, A. H. Price, A. A. Meharg, *Anal. Bioanal. Chem.,* 2012, **402,** 3275-3286.

[42] B. E. Etschmann, C. G. Ryan, J. Brugger, R. Kirkham, R. M. Hough, G. F. Moorhead, D. P. Siddons, G. De Geronimo, A. Kuczewski, P. Dunn, D. Paterson, M. D. de Jonge, D. L. Howard, P. Davey, M. Jensen, *Am. Mineral.,* 2010, **95***,* 884–887.

[43] B. E. Etschmann, E. Donner, J. Brugger, D. L. Howard, M. D. de Jonge, D. Paterson, R. Naidu, K. G. Scheckel, C. G. Ryan, E. Lombi, *Environ. Chem.*, 2014, **11**, 341-350.

[44] P. M. Kopittke, M. D. de Jonge, P. Wang, B. A. McKenna, E. Lombi, D. Paterson, D. L. Howard, S. A. James, K. M. Spiers, C. G. Ryan, A. A. T. Johnson, N. W. Menzies, *New Phytol.,* 2014, **201**, 1251-1262.

[45] C. M. Weekley, A. Shanu, J. B. Aitken, S. Vogt, P. K. Witting, H. H. Harris, *Metallomics*, 2014, DOI: 10.1039/c4mt00088a.

[46] L. Monico, K. Janssens, C. Miliani, B. G. Brunetti, M. Vagnini, F. Vanmeert, G. Falkenberg, A. Abakumov, Y. Lu, H. Tian, J. Verbeeck, M. Radepont, M. Cotte, E. Hendriks, M. Geldof, L. van der Loeff, J. Salvant, M. Menu, *Anal. Chem. (Washington, DC, U. S.),* 2013, **85**, 851-859.

[47] L. Monico, K. Janssens, E. Hendriks, B. G. Brunetti, C. Miliani, *J. Raman Spectrosc.,* 2014, DOI 10.1002/jrs.4548.

[48] M. Salomé, M. Cotte, R. Baker, R. Barrett, N. Benseny-Cases, G. Berruyer, D. Bugnazet, H. Castillo-Michel, C. Cornu, B. Fayard, E. Gagliardini, R. Hino, J. Morse, E. Papillon, E. Pouyet, C. Rivard, V. A. Solé, J. Susini, G. Veronesi, *J. Phys.: Conf. Ser., 2013*, **425,** 182004.

[49] D. Paterson, M. D. de Jonge, D. L. Howard, W. Lewis, J. McKinlay, A. Starritt, M. Kusel, C. G. Ryan, R. Kirkham, G. Moorhead, D. P. Siddons, *AIP Conf.* Proc., 2011, **1365**, 219-222.

[50] C. G. Ryan, D. R. Cousens, S. H. Sie, W. L. Griffin, G. F. Suter, E. Clayton, *Nucl. Instrum. Methods Phys. Res., Sect. B*, 1990, **47**, 55−71.

[51] C. G. Ryan, D. P. Siddons, R. Kirkham, P. A. Dunn, A. Kuczewski, G. Moorhead, G. De Geronimo, D. J. Paterson, M. D. de Jonge, R. M. Hough, M. J. Lintern, D. L. Howard, P. Kappen, J. Cleverley, *AIP Conf. Proc.,.* 2010, **1221**, 9-17.

[52] Y. Liu, F. Meirer, P. A. Williams, J. Wang, J. C. Andrews, P. Pianetta, *J. Synchrotron Radiat.*, 2012, **19**, 281-287.

[53] V. De Andrade, J. Ganne, B. Dubacq, C. G. Ryan, F. Bourdelle, A. Plunder, G. Falkenberg, J. Thieme*, J. Phys.: Conf. Ser.*, 2014, **499**, 012012.

[54] V. A. Solé, E. Papillon, M. Cotte, P. Walter, J. Susini, *Spectrochim. Acta B,* 2007, **62,** 63–68.

[55] B. Ravel, M. Newville, M. *J. Synchrotron Radiat.* 2005, **12,** 537–541.

[56] E. Hendriks, M. Geldof. In *Vincent Van Gogh Paintings 2: Antwerp & Paris, 1885-1888*, E. Hendriks, L. Van Tilborgh, Waanders Publishers, Amsterdam and Zwolle, 2011; pp 90-143.

[57] M. Vellekoop, M. Geldof, E. Hendriks, L. Jansen, A. de Tagle. *Van Gogh's studio practice;* Yale University Press, New Haven and London, 2013.

[58] Y. Liu, J. C. Andrews, F. Meirer, A. Mehta, G. S. Carrasco, P. Sciau, Z. Mester, P. Pianetta, *AIP Conf. Proc.,* 2011, **1365**, 357-360.

[59] B. Fayard, E. Pouyet, G. Berruyer, D. Bugnazet, C. Cornu, M. Cotte, V. De Andrade, F. Di Chiaro, O. Hignette, J. Kieffer, T. Martin, E. Papillon, M. Salomé, V. A. Solé, *J. Phys.: Conf. Ser.,* 2013, **425**, 192001.

[60] F. Meirer, Y. Liu, E. Pouyet, B. Fayard, M. Cotte, C. Sanchez, J. C. Andrews, A. Mehta, P. Sciau, *J. Anal. Atom. Spectrom.*, 2013, **28**, 1870-1883.

[61] P. Tack, J. Garrevoet, S. Bauters, B. Vekemans, B. Laforce, E. Van Ranst, D. Banerjee, A. Longo, W. Bras, L. Vincze, *Anal. Chem. (Washington, DC, U. S.),* **86**, 8791-8797.

Cr K-edge full spectral-XANES imaging based on the Maia X-ray detector array is proposed as a new data collection strategy for Cr speciation studies of chrome yellow-based paints in artworks by Vincent van Gogh